Strain engineering in gradient-structured metallic glasses for excellent overall water splitting

Chaoqun Pei [a,b,c,1], Shuangqin Chen [a,1,*], Jiuyuan Xie [c,h,1], Shidong Feng [d,1], Mingyuan Yu [e], Cheng Zhan [e,*], Yuyang Qian [c], Guannan Yang [i], Yuxuan Chen [d], Si Lan [a], Erjun Kan [e], Di Wang [f], Xiaoke Mu [f], Horst Hahn [f], Baoan Sun [b,c,*], Gerhard Wilde [a,g], Tao Feng [a,*]

[a] Herbert Gleiter Institute of Nanoscience, School of Material Science and Engineering, Nanjing University of Science and Technology, Nanjing 210094, China
[b] Institute of Physics, Chinese Academy of Sciences, Beijing 100190, China
[c] Songshan Lake Materials Laboratory, Dongguan, Guangdong 523808, China
[d] State Key Lab of Metastable Materials Science and Technology, School of Materials Science and Engineering, Yanshan University, Qinhuangdao, Hebei 066004 China
[e] School of Physics, Nanjing University of Science and Technology, Nanjing 210094, China
[f] Institute of Nanotechnology, Karlsruhe Institute of Technology, Karlsruhe 76021, Germany
[g] Institute of Materials Physics, University of Münster, Münster 48149, Germany
[h] School of Physics and Materials Science, Guangzhou University, Guangzhou 510006, China
[i] State Key Laboratory of Precision Electronic Manufacturing Technology and Equipment, School of Electromechanical Engineering, Guangdong University of Technology, Guangzhou 510006, China

Metallic glasses (MGs) represent cutting-edge electrocatalysts due to their distinctive disordered atomic structure. However, enhancing the activity of MG catalysts poses a significant challenge. In this study, we present an innovative gradient structure design aimed at introducing strain effects into non-noble $Ni_{40}Fe_{40}P_{20}$ MG wires, resulting in a substantial enhancement of their water electrolysis efficiency. Our novel design strategy has been successfully implemented in various composition MG wires fabricated using the Taylor–Ulitovsky (TU) method. The gradient-structured metallic glasses (GS-MGs) enable the attainment of large and consistent surface tensile strain, which in turn modifies the electronic structure, leading to a remarkable improvement in catalytic performance. Furthermore, employing free-standing $Ni_{40}Fe_{40}P_{20}$ GS-MGs with a fully three-dimensional nanoporous structure as both cathode and anode in the overall water-splitting cell has achieved breakthrough performance in alkaline media. Notably, the cell exhibits significantly reduced potentials of only 1.378 V and 1.682 V at current densities of 10 mA cm^{-2} and 1000 mA cm^{-2}, respectively, surpassing precious metal catalysts and previously reported advanced electrocatalysts. This study demonstrates that strain engineering induced by gradient structures is a universal and effective strategy for enhancing the catalytic performance of MGs. It introduces a new paradigm for the development of high-efficiency water splitting applications.

Keywords: Gradient structure; Metallic glass; Strain engineering; Catalytic performance; Overall water splitting

* Corresponding authors.
E-mail addresses: Chen, S. (chensq-hgi@njust.edu.cn), Zhan, C. (czhan@njust.edu.cn), Sun, B. (sunba@iphy.ac.cn), Feng, T. (tao.feng@njust.edu.cn).
[1] These authors contributed equally to this work.

Introduction

Water electrolysis stands as a pivotal pathway in the quest for sustainable and renewable energy sources, particularly in the generation of hydrogen, poised to supplant conventional fossil fuels [1,2]. However, despite its potential, the current global production of hydrogen through water electrolysis remains severely constrained, accounting for less than 4 % of total hydrogen output. This limitation stems from the exorbitant capital expenditure associated with precious metal catalysts and the substantial electricity consumption required for the electrolysis process [3,4]. Consequently, the pursuit of highly efficient and cost-effective catalysts for water electrolysis remains a formidable challenge.

Metallic glasses (MGs), hailed for their remarkable efficiency, durability, and cost-effectiveness, are promising contenders to address the challenges of both capital and electricity consumption. Their allure lies in the amalgamation of virtues, including a high density of low-coordination sites, elevated Gibbs free energy, and synergistic effects [5–8]. For instance, Ir-Ni-Ta MGs have showcased exceptional catalytic prowess for the hydrogen evolution reaction (HER), achieving superior stability with an ultralow Ir loading in acidic media [9]. Similarly, Ni-Mo-Nb MGs have demonstrated highly active and stable performance for the hydrogen oxidation reaction (HOR) in alkaline electrolytes, outperforming even commercial Pt catalysts. This superiority is attributed to the pronounced synergies between nickel, molybdenum, and niobium, alongside the favorable atomic configurations across multiple length scales [10]. However, the extensive disorder in the atomic arrangement of MGs poses a significant challenge in tailoring their catalytic performance. Without deliberate structural interventions such as phase modulation, surface facet engineering, or defect manipulation, the pursuit of high-efficiency MG catalysts has predominantly relied on compositional adjustments. Yet, this approach has rendered them mere 'bench-warmers' in the fervent battleground of electrocatalysis. Thus, the imperative emerges to innovate novel strategies that transcend compositional tinkering and unlock the full catalytic potential of MGs, propelling them to the forefront of electrocatalytic innovation [11].

Delving into advanced methodologies to enhance the catalytic activity of MGs is not merely a matter of practical significance but also an imperative endeavor to unravel the intricate structure-performance dynamics governing their efficacy. Understanding these nuances paves the way for informed structural designs aimed at producing more active MG catalysts. Recently, strain engineering, involving the introduction of compressive or tensile surface strain, has emerged as a highly potent technique for substantially augmenting the electrocatalytic prowess of crystalline materials [12–17]. As an illustration, the lattice strain characterized by a core–shell structure in Pt-based catalysts induces a noteworthy alteration in the electronic band structure of platinum, thereby diminishing the chemisorption affinity of oxygenated species [18]. This phenomenon serves to amplify the catalytic activity significantly. The imposition of compressive surface strains on Pt-based catalysts yields stable Pt (1 1 0) facets, exhibiting remarkable specific and mass activities in the oxygen reduction reaction (ORR). These activities reach 7.8 mA cm^{-2} and 4.3 A mg^{-2} of Pt, respectively, at 0.9 V versus the reversible hydrogen electrode (RHE). Notably, these catalysts demonstrate exceptional durability, enduring 50,000 voltage cycles with negligible activity decay [15]. Exploiting tunable, wide-range strain engineering of spinel oxides (such as $NiFe_2O_4$) has been suggested to effectively reduce the energy barrier associated with the rate-determining step in the oxygen evolution reaction (OER). This approach enables the achievement of a remarkably low overpotential of 180 mV at 10 mA cm^{-2} [19]. In essence, strain engineering possesses the capability to alter the electronic structure of catalytic materials by adjusting the interatomic spacing, a concept that transcends traditional crystallology. Yet, the feasibility and mechanisms of applying strain engineering to MGs and its potential to enhance catalytic performance remain elusive. This ambiguity persists due to the intricate and enigmatic nature of amorphous structures.

Here, we unveil a cutting-edge approach by engineering advanced gradient structure to harness the power of strain manipulation within MGs, thus revolutionizing their catalytic efficiency. Gradient-structured metallic glasses (GS-MGs) possess a unique characteristic wherein the interatomic spacing, or atomic packing density, gradually shifts from the surface towards the interior, creating a significant distribution of strain within the MGs. Fabricated into wire shapes using the Taylor–Ulitovsky (TU) method, these GS-MGs exhibit a notable disparity in density between their surfaces and centers. In particular, the $Ni_{40}Fe_{40}P_{20}$ (NFP) GS-MG wire showcases a remarkable enhancement in catalytic performance for both the HER and OER in alkaline solutions compared to conventional MGs, such as melt-spun ribbons with identical composition. Density functional theory (DFT) calculations shed light on the underlying mechanisms, revealing that the expansion of interatomic spacing in NFP MG leads to an upward shift of the d-band center, facilitating enhanced interactions with adsorbates—an advantageous trait for HER and OER reactions.

The versatility of this groundbreaking strategy is further demonstrated through the fabrication of GS-MG wires using nickel-based, palladium-based, and cobalt-based compositions. Additionally, the gradient structure facilitates the formation of a fully three-dimensional nanoporous (3D-NP) architecture within NFP GS-MG, achieving a breakthrough performance in overall water-splitting. Notably, the NFP GS-MG exhibits potentials as low as 1.378 V and 1.682 V at current densities of 10 mA cm^{-2} and 1000 mA cm^{-2}, respectively. These compelling results underscore the viability of extending strain engineering strategies to MG catalysts. Moreover, the gradient structure design offers a universal and effective approach to harness strain engineering, thereby elevating the catalytic performance of MGs to unprecedented levels.

Results and discussion

The schematic representation in Fig. 1a (left) illustrates the synthetic procedure for producing NFP MG wires utilizing the Taylor-Ulitovsky (TU) method [20], also known as the glass coating method. Initially, NFP precursor alloy ingots are subjected to melting within a borosilicate glass tube via induction heating, leading to the formation of a molten pool. This molten NFP alloy

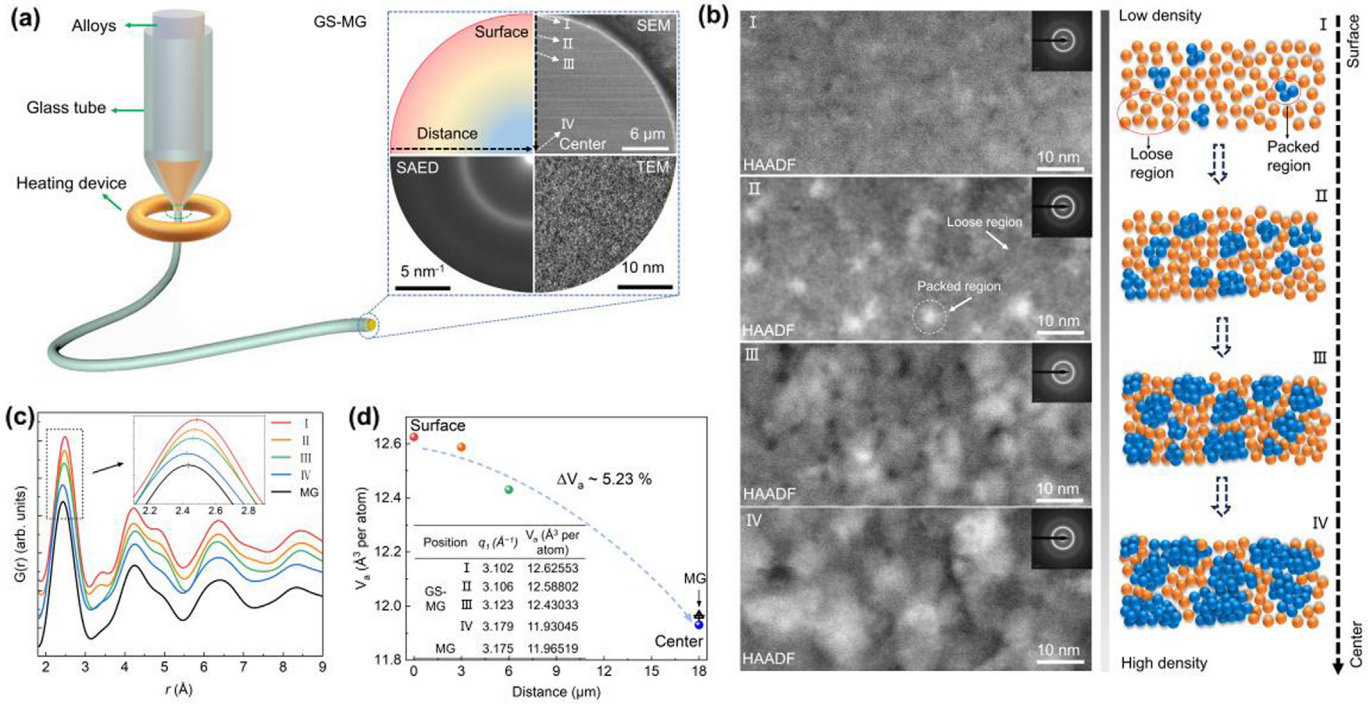

FIG. 1

Structural characterizations of NFP GS-MG by TEM. (a), Schematic diagram indicating the fabrication of GS-MG wires with the corresponding structure characterizations. **(b),** HAADF-STEM results of NFP GS-MG from four regions (labeled I, II, III, IV) from (a) with the corresponding structural models. **(c),** Corresponding radial distribution functions, *G*(r), as a function of the distance, r, calculated from the SAED of TEM of four regions in NFP GS-MG. **(d),** Local atomic volume, V_a, of four regions in NFP GS-MG.

is then drawn through the glass tube under a controlled traction force, resulting in the formation of the MG wire due to rapid cooling. Fig. 1a (right) depicts a schematic illustrating the gradient structure within the MG wire, along with its corresponding structural features. Scanning Electron Microscopy (SEM) image displays a 1/4 cross-section of NFP MG wire, approximately 35 μm in diameter. The vitreous nature of the wires is confirmed by High-Resolution Transmission Electron Microscopy (HR-TEM), Selected Area Electron Diffraction (SAED), and X-ray Diffraction (XRD) analyses (refer to Fig. S1a). The Energy-Dispersive X-ray Spectroscopy (EDS) mapping conducted within the SEM (refer to Fig. S2a) showcases the detailed surface morphology of NFP MG wire, emphasizing the homogeneous distribution of its constituent elements, namely Ni, Fe and P.

Fig. 1b presents the outcomes of High-Angle Annular Dark-Field Scanning Transmission Electron Microscopy (HAADF-STEM) at four distinct regions spanning from the surface to the center of NFP MG wire (denoted as Ⅰ, Ⅱ, Ⅲ, and Ⅳ, as indicated in the SEM image of Fig. 1a and Fig. S3). Notably, the SAED patterns obtained from all four regions unequivocally affirm the amorphous nature of NFP MG wire. To our surprise, the HAADF images captured in different regions are significantly distinguished, which implies a structural change from the surface to the center. Since HAADF-STEM is sensitive to the local chemistry and density, the heterogeneous contrast implies an inhomogeneous distribution of density or chemistry in MGs [21,22]. STEM EDS mappings in bright field (BF) and dark field (DF) modes (in Fig. S4–S7) show no visible chemical variation correlated with the heterogeneity of the HAADF-STEM signal, which indicates that the contrast mainly originates from the difference of atomic packing densities. Thus, bright areas in the HAADF-STEM image represent regions where atoms are more closely packed, while dark areas are more loosely packed regions. Based on the observations derived from the HAADF-STEM images acquired across regions Ⅰ to Ⅳ, a progressive enlargement of bright areas is noted, indicating a corresponding increase in atomic packing density from the surface towards the center of NFP MG wire. The atomic structure diagrams representing different regions are depicted on the right side of Fig. 1b for clarity. Fig. 1c illustrates radial distribution functions (RDFs, *G*(r)) computed from the SAED patterns obtained via TEM analysis across regions Ⅰ, Ⅱ, Ⅲ, and Ⅳ of the NFP MG wire (refer to Fig. S3). Analysis of the RDFs reveals a shift in the positions of the first peaks towards higher distance (r) values, signifying an augmentation in average atomic distances from the wire's center (region Ⅳ) towards its surface (region Ⅰ). Additionally, the local atomic structure from the wire's surface to its center is characterized by determining the atomic volume (V_a) utilizing the structure factor *S*(q) (refer to Fig. S8) [23]. Fig. 1d presents the surface V_a of NFP MG wire, estimated at approximately 12.626 Å^3 per atom, indicating a lower atomic packing density of about 5.23 % compared to the center ($V_a \approx$ 11.930 Å3 per atom). This discrepancy corresponds to a surface tensile strain of approximately 1.91 %. Consequently, the gradient structure of NFP MG wire is confirmed, with the atomic packing density progressively increasing from the surface towards the center.

The gradient feature of NFP GS-MG is also identified by nano-indentation. As shown in Fig. 2a, by nano-indentation testing,

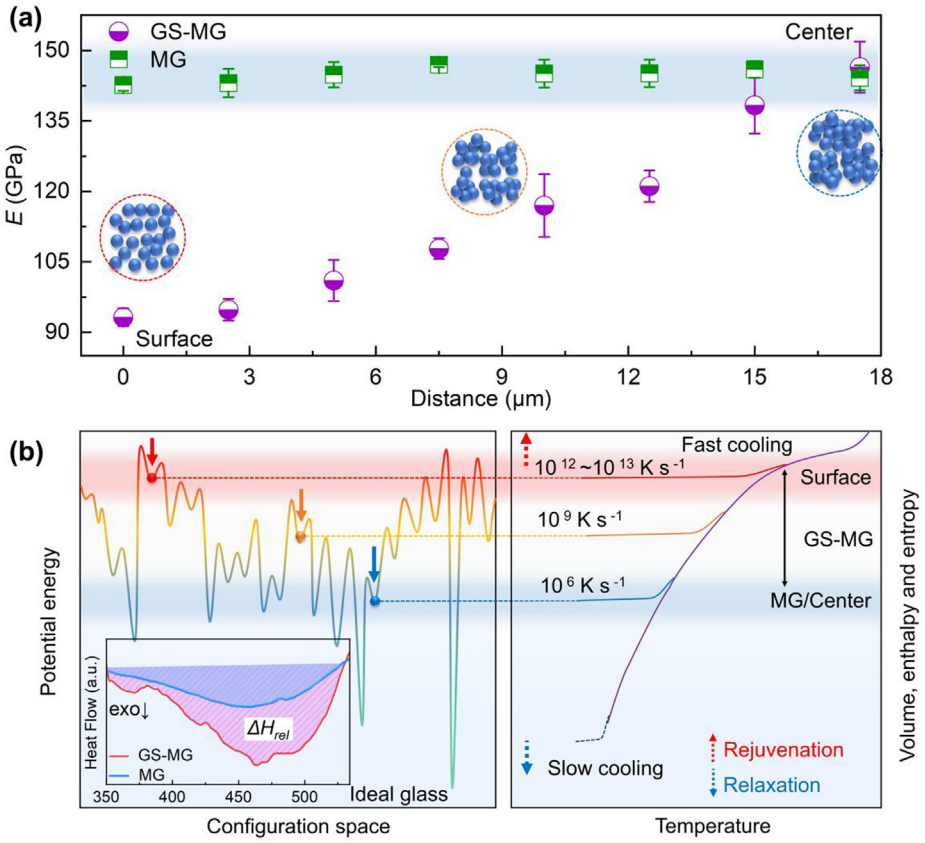

FIG. 2

Young's modulus and thermodynamic characterizations of NFP GS-MG. (a), Young's modulus of NFP GS-MG and MG obtained by nano-indentation. (**b),** Schematic diagram of the potential energy landscape of NFP GS-MG from the surface to the center.

the Young's modulus (E) from the surface to the center of NFP GS-MG was measured and clearly revealed a gradient-like variation. Specifically, the modulus at the surface is ~ 93.21 ± 1.91 GPa, which is much lower (ΔE ~ 36 %) than that in the center of NFP GS-MG (~ 146.45 ± 5.47 GPa). However, the modulus of the conventional MG (melt-spun ribbon with the identical composition) shows a uniform value of ~ 144.73 ± 3.01 GPa. According to the empirical correlation between E and the glass transition temperature (T_g) [24], a gradient structure of NFP GS-MG is revealed and a reduced T_g at the surface of the GS-MG can be deduced with $T_{g\text{-surface}} \cong 0.64\ T_{g\text{-center}}$, indicating an extremely high surface energy state. Moreover, E is also regarded as the descriptor of atomic packing density. The gradient distribution of E in NFP GS-MG implies a gradient atomic packing structure, which is confirmed by analyzing the structures of NFP GS-MG. Moreover, Differential Scanning Calorimetry (DSC) measurements were performed to determine the energy state of NFP GS-MG and the conventional MG. The NFP GS-MG shows a lower T_g ~ 531 K and T_x ~ 635 K (initial crystallization temperature) in comparison with the MG with T_g ~ 612 K and T_x ~ 646 K, respectively, implying its higher energy state (Fig. S9). In addition, the NFP GS-MG displays a notable exothermic process at sub-T_g temperatures that is much less pronounced for the MG with identical composition, as shown in the inset of Fig. 2b. To acquire quantitative information on the energy states of NFP GS-MG and MG, the relaxation enthalpy ΔH_{rel} [25–28], measured from the sub-T_g exothermic peaks, is calculated to be ~ 0.99 kJ/mol, which is much higher than that of the MG (~ 0.42 kJ/mol), further confirming the higher energy state of NFP GS-MG. Combining all of the above experimental results—i.e., the larger global relaxation enthalpy ΔH_{rel}, the reduced modulus, and the enlarged average atomic distance—not only demonstrate the gradient atomic structure of NFP GS-MG, but also indicate a gradient energy structure from the surface to the center. In order to clearly describe and quantify the energy distribution in NFP GS-MG, the concept of an effective cooling rate is adopted to present the rejuvenation degree from the surface to the center. Fig. 2b shows the schematic diagram of the potential energy landscape of NFP GS-MG from the surface to the center. The effective cooling rate can be calculated from ΔH_{rel} [25] and estimated from the variation of Young's modulus [29]. The average effective cooling rate of NFP GS-MG calculated from the ΔH_{rel} (the inset of Fig. 2b) is about 10^9 K/s. The energy state of the central region of the GS-MG is similar to the MG, where the effective cooling rate is estimated at about 10^5 ~ 10^6 K/s. Thus, the surface energy of the GS-MG is much higher than that of the average material. The effective cooling rate for the surface is estimated to be as high as 10^{12} ~ 10^{13} K/s, which is approaching the highest reported cooling rates equivalent to irradiation [29]. These high effective cooling rates that apply at the surface serve to achieve extremely high surface energy values.

The origin of the distinct gradient structure is attributed to the unique preparation process of the MG wires (see details in the Methods section, Fig. 1a, and Movie S1). The TU method is a vital

method for fabricating metallic wires featured with a glass coating. During the preparation process of the glass-covered MG wires, radial and azimuthal internal stresses and temperature fields are induced, determining the structure and mechanical properties. Specifically, on the one hand, the local thermal diffusivity of the MG wires is related to the radius, thereby forming a radially varying temperature field from the inside to the outside, resulting in a radius dependence of the local cooling rates [30]. On the other hand, a negative stress in the radial direction will be generated due to the mismatch of the coefficients of thermal expansion between the glass coating and the MG wires (Fig. S10). That negative stress leads to a looser atomic packing of the surface structure with associated high local energy. The negative stress coupled with the temperature field distribution leads to radial symmetry associated with a gradient structure consisting of a cylindrical inner core with a lower-energy state and a cylindrical outer shell with higher-energy state. Coincidentally, similar gradient structure materials can also be synthesized by adjusting processing conditions of cryogenic thermal cycling and fast cooling, which was recently reported by Jiang et al [31]. Inspired by these encouraging experimental results, we further confirmed the generality of this method to prepare gradient structure materials. For example, we also demonstrate the universality of the gradient structure for different types of Ni-based ($Ni_{77}P_{23}$) and Pd-based ($Pd_{40}Ni_{10}Cu_{30}P_{20}$) GS-MG wires by nano-indentation in Fig. S11. The radial distribution functions calculated from SAED of Ni-based GS-MGs, $G(r)$, suggest the same phenomenon as observed for NFP GS-MG (Fig. S12).

MGs characterized by lower atomic packing density are anticipated to demonstrate enhanced catalytic performance owing to their increased specific volume, elevated density of low-coordination sites, and consequently, a higher density of potential active sites. As depicted in Fig. 3a, the NFP GS-MG exhibits markedly improved catalytic activity for the OER, showcasing an overpotential of 313 mV at a current density (j) of 100 mA/cm^2, which is substantially lower than that of the corresponding conventional MG (411 mV). Furthermore, the NFP GS-MG demonstrates excellent performance for the HER in Fig. 3b, exhibiting an overpotential of 308 mV at a current density of 100 mA/cm^2, while the conventional MG displays notably inferior performance with an overpotential of 569 mV at the same current density.

To validate the universality of this unique gradient structure with a lower density near the surface, which imparts superior catalytic performance, GS-MGs based on Fe, Ni, Co, and Pd were synthesized, and their catalytic performance monitored (as

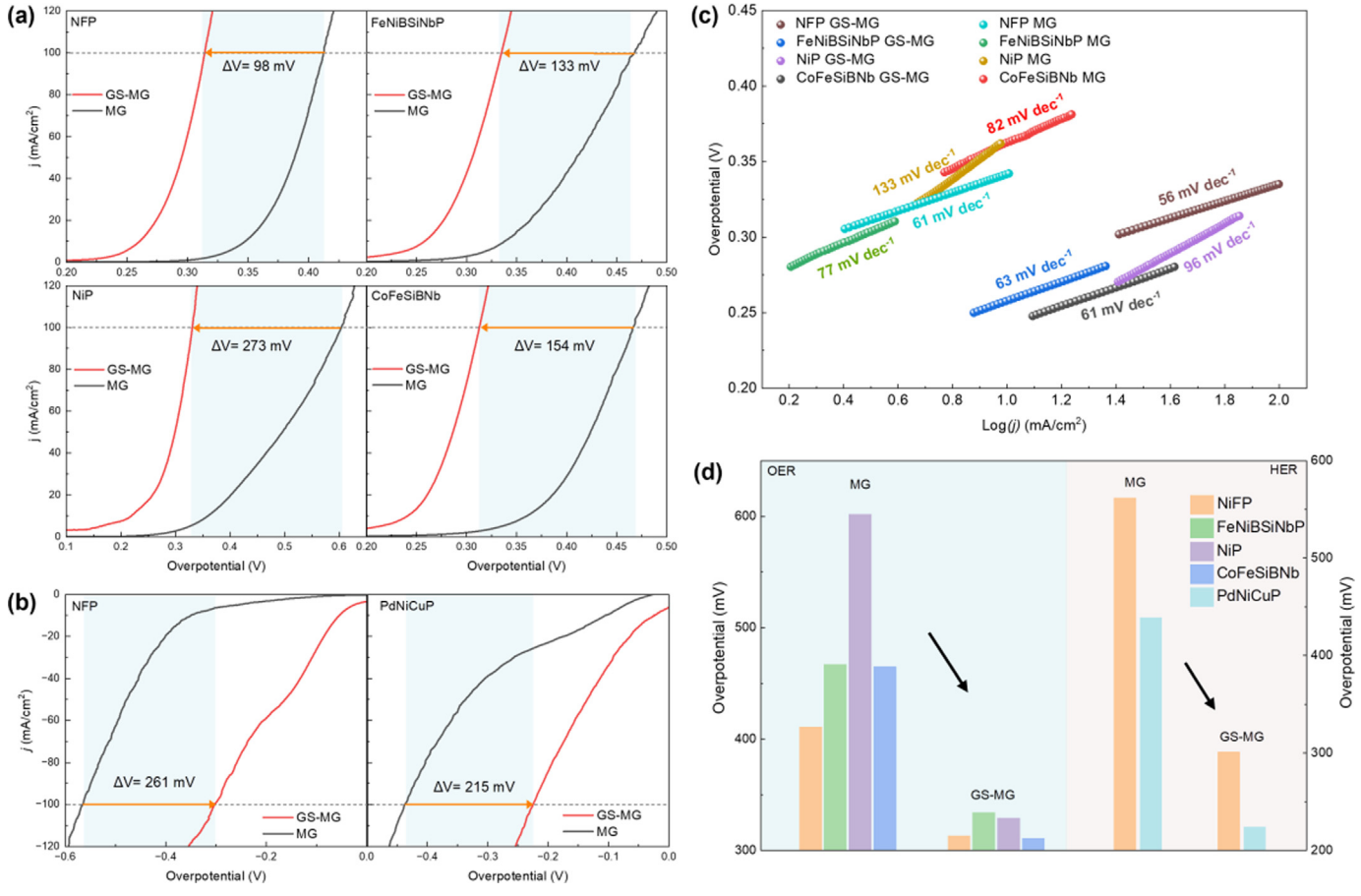

FIG. 3

Catalytic performance of GS-MGs and MGs with various compositions. (a), OER polarization curves of NFP, FeNiBSiNbP, NiP and CoFeSiBNb GS-MGs and MGs. (**b),** HER polarization curves of NFP and PdNiCuP GS-MGs and MGs. (**c),** Tafel slopes of different electrocatalysts for OER. (**d),** Comparison of the catalytic performance (OER and HER) at a current density of 100 mA cm^{-2} for GS-MGs and MGs.

shown in Fig. 3a and 3b). As anticipated, the Pd-based GS-MG demonstrates significantly enhanced HER performance with a low overpotential of 222 mV @ j = 100 mA cm^{-2} compared to its corresponding conventional MG (437 mV) (Fig. 3b). Similarly, Fe-based, Ni-based, and Co-based GS-MGs exhibit markedly enhanced OER performance with overpotentials of 334 mV, 329 mV, and 312 mV @ j = 100 mA cm^{-2}, respectively, compared to their corresponding MGs with overpotentials of 467 mV, 602 mV, and 466 mV, respectively (Fig. 3a). Fig. 3c presents Tafel curves of various GS-MGs and their corresponding MGs concerning OER. It is evident that all GS-MGs (including NFP, Fe-based, Ni-based, and Co-based) exhibit considerably lower Tafel slopes compared to MGs, indicating more favorable reaction kinetics for GS-MGs. Additionally, all GS-MGs demonstrate smaller diameters of semicircles on Nyquist plots and lower values of charge transfer resistance (R_{ct}) (Fig. S13) in comparison with their corresponding MG samples, further affirming the superior and faster kinetics of GS-MGs for electrochemical catalysis. In summary, through comparative analysis of overpotentials at the same current density of 100 mA cm^{-2} (Fig. 3d), it is unequivocally demonstrated that GS-MGs exhibit superior catalytic performance compared to MGs, primarily manifested by a substantial reduction in overpotential and a notable enhancement in reaction kinetics.

To deeply understand the effect of the atomic packing density (change of packing density is realized by tuning the lattice strain in xy directions) of a MG on the catalytic performance, DFT calculations were conducted to reveal the underlying mechanisms. According to the experimental characterization, the atomic structure models of amorphous NFP ($Ni_{40}Fe_{40}P_{20}$) with different atomic packing densities are constructed (in Fig. 4a and Fig. S14 and Methods section for detalis), including the original density (0 %), reduced density (RD) of 2 %, 5 % and 10 %, respectively. The amorphous structure is generated by *ab initio* molecular dynamics (AIMD) calculation at 2000 K on the original $Ni_{40}Fe_{40}P_{20}$ crystal surface. More than twenty configurations were randomly selected for further catalytic simulation, as shown in Fig. S14-S18 (more details are provided in the Supplementary Information). To obtain information on the electronic structure of NFP MGs with four different densities (RD-0 %, RD-2 %, RD-5 % and RD-10 %), the partial density of states (PDOS) of each elements (Ni, Fe and P) and total were calculated, as shown in Fig. 4a. The d-band center is strongly associated with the adsorption energy of the adsorbates. When the d-band center is closer to the Fermi level (E_F), the d orbital of catalysts exhibits stronger binding ability to the adsorbates, which significantly affect the catalytic performance [32]. With the atomic packing density decrease from RD-0 % to RD-10 %, the d-band center of Ni-3d

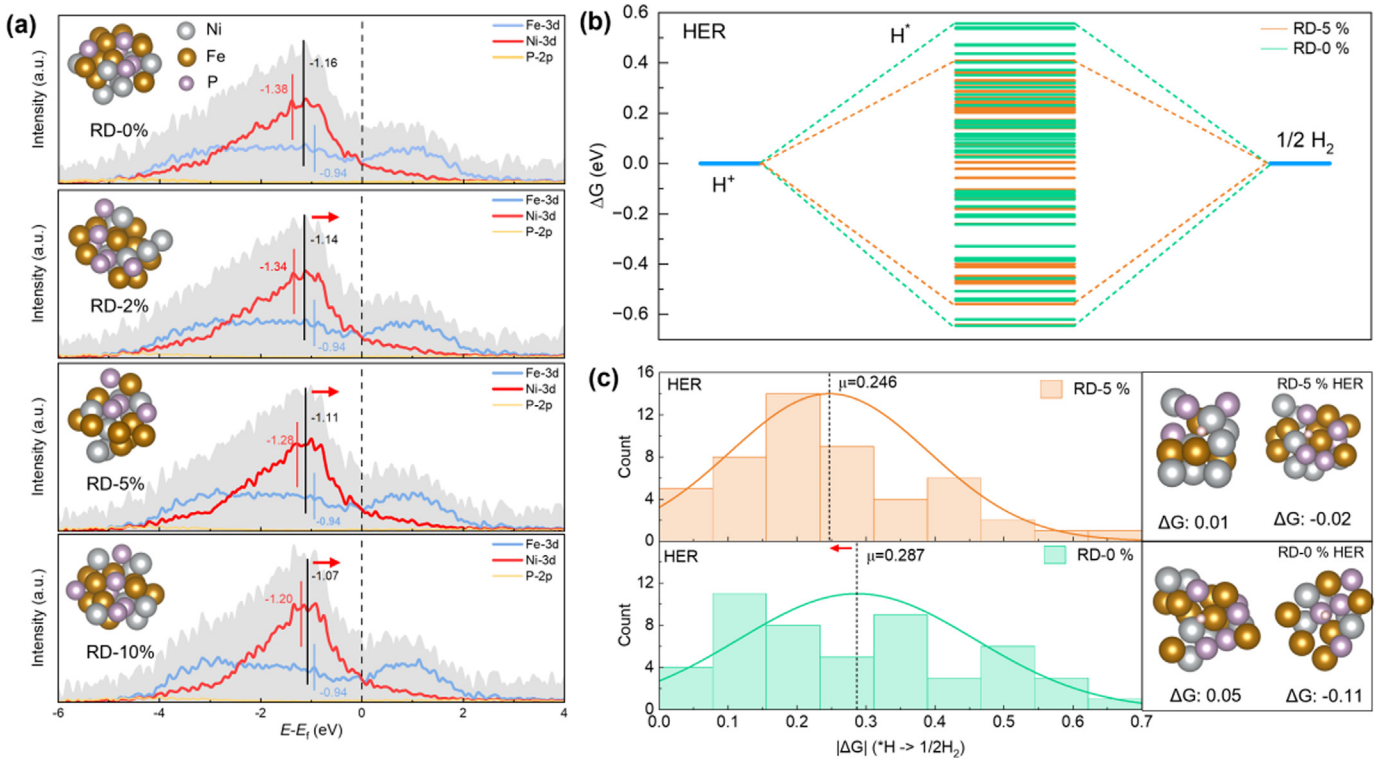

FIG. 4

DFT simulations of NFP MG with different atomic packing densities. (a), The PDOS results for the Ni, Fe and P active sites with different atomic packing densities of NFP MGs. The black dashed line indicates the Fermi level, black solid lines highlight the corresponding total d-band centers of different densities. **(b),** The comparison of Gibbs free energy (ΔG) profiles for various catalytic sites of NFP clusters with two different densities (RD-0% and RD-5%) for HER. **(c),** Gibbs Free energy distributions of H* adsorption/desorption step (Heyrovsky step) of two different densities (RD-0% and RD-5%) for HER, the right clusters for some examples of active sites for HER.

orbital exhibit a prominent upshift from −1.38 eV to −1.20 eV and gradually approach the E_F, which hints that the atomic packing density should have significant impact on the catalytic activity. However, the d-band center of Fe shows very little change, which indicates that the change of the catalytic activity is more likely to be attributed to the Ni d orbital. The P-3p orbital locates at positions considerably below E_F, indicating its electron-rich feature, which could balance the surface electroactivity to suppress the over-binding effect by Ni-H and Ni-O. Additionally, the total d-band center also exhibit a prominent upshifting from −1.16 eV to −1.07 eV with the attenuation of the average atomic packing density from RD-0 % to RD-10 %. Therefore, reducing the atomic packing density of MGs will be conducive to enhance the catalytic performance. To further determine the fundamental correlation between the electrocatalytic mechanisms and the atomic packing density of MGs, we carried out free energy calculation on various active sites for both HER and OER (Fig. 4b, Fig. S19). We calculated the HER and OER reaction free energy of various MG models in different atomic packing densities (RD-0 % and RD-5 %). For HER simulation, the Gibbs free energy (ΔG) of *H adsorption were systematically calculated in Fig. 4b and the corresponding MG configurations are shown in Fig. S15–S16. We found that the active sites in RD-5 % (the range of orange dash line in Fig. 4b) models showed the relatively lower ΔG values than that of original (RD-0 %, the range of green dash line in Fig. 4b) model, as shown in Fig. S19a–c. To further quantify the ΔG with two densities for HER, statistical distribution of ΔG from different selected models was displayed in Fig. 4c. The contribution of the ΔG of RD-5 % is lower with a mean of ∼ 0.246 eV, which is much lower than that of the original (0.287 eV). Such results indicate that the attenuation of atomic packing densitiy in NFP clusters can promote the HER activity, which agrees well with our experimental finding in Fig. 3b. We also calculated the OER free energies at various active sites with different atomic packing densities (RD-0 % and RD-5 %) from our selected MG models, as shown in Figs. S17–S18. Four steps of the OER process were included in our calculation and the free energy of each step was shown in Fig. S17 (RD-5 %) and Fig. S18 (original model, RD-0 %). According to the Volcano relation in early studies, the value of $G_{*O} - G_{*OH}$ is strongly correlated to the overpotential of OER in transition metal oxide electrocatalysts with the best performance located at $G_{*O} - G_{*OH}$ = 1.6 eV [33,34]. By comparing the $G_{*O} - G_{*OH}$ of MG models with original packing density and reduced packing density in Fig. S19d-f, we found that the overall distribution of $G_{*O} - G_{*OH}$ in RD-5 % is closer to the 1.6 eV than that in original packing density (unstrained model), which means that lower packing density could statistically improve the OER performance of MG. Therefore, DFT calculations demonstrate that reducing the atomic packing density of MGs could improve both HER and OER performance, which is consistent with the experimental observations.

We further obtained a 3D nanoporous (3D-NP) structure of GS-MG for promoting the catalytic performance by dealloying (for details see the Methods section and Fig. S20). Fig. 5a shows the 3D-micrograph of NFP 3D-NP GS-MG obtained by Nano-CT. The surface of NFP 3D-NP GS-MG has a distinct porous structure with a pore size of around 50–200 nm, as shown in Fig. 5b. We also conducted a comparative analysis of the composition of NFP 3D-NP GS-MG by EDS mapping (Fig. S21-S22). The surface of NFP 3D-NP GS-MG shows an enrichment of O due to oxidation, with a slightly decrement of Fe and P and an increase of Ni. These composition changes can be attributed to the partial dissolution of Fe in the acidic solution during the process of dealloying. The SEM surface topographies in Fig. 5b–c clearly reveal the presence of distinctive features between the surface and the internal corrosion morphology, which can be attributed to the gradient structure of the MG wire. In order to observe the detailed structure of NFP 3D-NP GS-MG, an enlarged micrograph of the cross-section form Fig. 5a is exhibited in Fig. 5d marked by the orange region, which clearly exhibits a nano-porous morphology. With the Nano-CT results, a gradient of porosity is observed from the surface to the center of the wire in Fig. 5e (with a variation of the gray value from region Ⅰ, Ⅱ and Ⅲ), which may be related to the impact of the pre-existing gradient structure on dealloying. We further examined the morphology of NFP MG ribbon after dealloying. Unsurprisingly, we observed that NFP MG did not exhibit the similar 3D porous structure as GS-MG after corrosion. Instead, only a shallow porous corrosion layer appeared on its surface (∼ 500 nm), as shown in Fig. S23. Therefore, we conclude that the gradient structure facilitates the gradual penetration of the corrosion solution from the surface to the interior during the dealloying process, potentially creating differences in solution penetration rates between the surface and interior, which may account for the distinct structural features observed in NFP 3D-NP GS-MG. Additionally, we evaluated the catalytic performance of NFP 3D-NP GS-MG catalysts. As shown in Fig. 5f, the NFP 3D-NP GS-MG displays ultra-low overpotentials of 228 mV and 280 mV for OER at current densities (j) of 10 and 100 mA cm^{-2}, repectively, which shows a significant improvement of the performance compared to those of precious metal oxide RuO_2 (340 mV@10 mA cm^{-2}, Fig. S24a), NFP MG (411 mV), and the original NFP GS-MG (313 mV) for achieving current densities of 100 mA cm^{-2}. Moreover, the NFP 3D-NP GS-MG exhibits the smallest Tafel slope (37.75 mV dec^{-1}), compared to both MGs and commercial RuO_2, suggesting its fastest reaction kinetics for OER (Fig. S25a). Besides of OER, the NFP 3D-NP GS-MG also shows superior performance for HER. Surprisingly, as shown in Fig. 5g, the NFP 3D-NP GS-MG only requires 44 mV and 230 mV at current density of 10 and 100 mA cm^{-2}, respectively, which is much lower than that of the original GS-MG (308 mV), MGs (569 mV) and even lower than commercial precious Pt/C (254 mV, Fig. S24b) at current density of j = 100 mA cm^{-2}. Correspondingly, the smallest Tafel slope of 36 mV dec^{-1} of NFP 3D-NP GS-MG also demonstrates its fastest reaction kinetics for HER (Fig. S25b). The EIS results obtained on NFP 3D-NP GS-MG (Fig. S25c) exhibit a smaller radius of the Nyquist plots than MG, which is conducive to the enhancement of the charge transport and the improved catalytic effect [49]. To investigate the stability for both OER and HER, the chronopotentiometry tests (Fig. S26) were carried out.The NFP 3D-NP GS-MG exhibits a high stability with a negligible decrease of the current density after 100 h @ U_{OER} = 0.68 V and U_{HER} = −1.2 V, respectively. To our surprise, we found that the performance of HER has significantly improved after 100 h of chronopotentiometry test (Fig. S26c), indicated by the overpotential decrease to 23 mV at a current

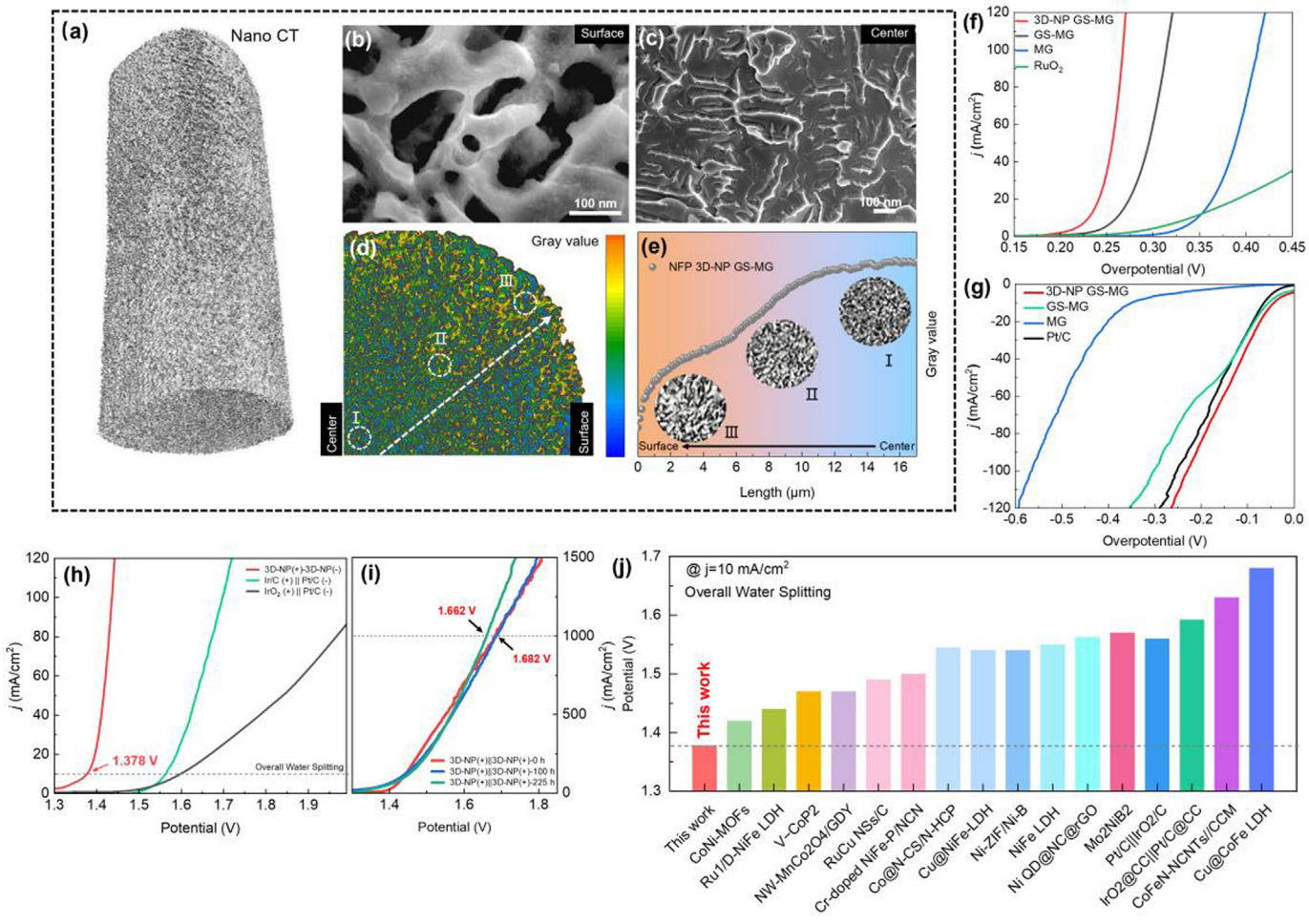

FIG. 5

Structure characterization and Catalytic performance of NFP 3D-NP GS-MG. (a)-(e), 3D topography of NFP 3D-NP GS-MG wire by SEM and Nano-CT. (f), OER polarization curves of NFP 3D-NP GS-MG. (g), HER polarization curves of NFP 3D-NP GS-MG. (h), Polarization curves of NFP 3D-NP GS-MGs for overall water splitting obtained by a two-electrode system. (i), Polarization curves at large current densities of 1000 mA cm^{-2} of NFP 3D-NP GS-MGs for overall water splitting before and after stability testing. (j), Comparison of the cell voltages at 10 mA cm^{-2} for NFP 3D-NP GS-MGs with reported bi-functional electrocatalysts [35–48].

density of 10 mA cm^{-2}. The electrochemically active surface area (ECSA) of NFP 3D-NP GS-MG was evaluated by the double-layer capacitance (C_{dl}) from CV curves in the non-Faradaic region (Fig. S27). It is found that the GS-MG with large C_{dl} value (7.35 mF cm^{-2}), expose more active sites and therefore exhibit a higher activity in comparison to MG (1.93 mF cm^{-2}) (Fig. S27d), demonstrating the advanced merits of the low density near the surface of the gradient structure for catalysis. Moreover, the NFP 3D-NP GS-MG exposes the highest density of active sites, as indicated by the highest C_{dl} value of 15.51 mF cm^{-2}. Therefore it exhibits the highest activity in comparison to both GS-MG and MG. X-ray photoelectron spectroscopy (XPS) analysis of NFP 3D-NP GS-MG further reveals substantial changes in the valence states of Ni, Fe, and P following the dealloying process (Fig. S28). Notably, distinct peaks corresponding to Ni^{2+}, Fe^{3+}, and PO_4^{3-} emerge after dealloying. These peaks are attributed to the formation of (NiFe)OOH-P during the OER [50–52], which is conducive to generate a considerable number of active sites, significantly enhancing the catalytic performance.

Inspired by the superior hydrogen and oxygen evolution performance of NFP 3D-NP GS-MG, a dual-electrode configuration electrolyser for overall water splitting (Fig. S29) was assembled by 3D-NP GS-MGs as both anode and cathode. The polarization curves of the as-prepared 3D-NP GS-MG||3D-NP GS-MG dual-electrode system are displayed in Fig. 5h and 5i. It only requires ulta-low cell voltages of 1.378 and 1.436 V to reach current densities (*j*) of 10 and 100 mA cm^{-2}, respectively, which are much lower values than the cell voltage of 1.56 V for Ir/C||Pt/C (Fig. 5h), or IrO_2||Pt/C (1.59 V) (commercial catalysts) [53]. In order to further evaluate the overall water splitting reactivity, we calculated the Faraday Efficiency (FE) by detecting H_2 as the product at a constant current of 50 mA of NFP 3D-NP GS-MG electrode for the overall water splitting. The gathered H_2 gas volume suggests its FE up to 99.3 %, as shown in Fig. S30.

In particular, the integrated water-splitting cell incorporating NFP 3D-NP GS-MGs achieved a stable current density of 500 mA/cm^2 for more than 225 h without discernible degradation (Fig. S31). Post-chronoamperometric testing for 225 h, LVS (Linear Voltammetry Scans) were conducted to corroborate the

stability, revealing a voltage requirement as low as 1.662 V to attain j = 1000 mA/cm^2 (Fig. 5i), which even outperforms the original one. Comparatively, in the initial stages of operation, the NFP 3D-NP GS-MG||3D-NP GS-MG configuration not only demonstrated the lowest cell voltage (1.378 V @ 10 mA/cm^2) (Fig. 5j) but also exhibited one of the smallest potentials at high current densities (1.682 V @ 1000 mA/cm^2) (Fig. 5i). Given the application of high current densities in industrial water electrolyzers, such as anion exchange membrane water electrolyzers (AEMWEs) operating around 1000 mA/cm^2, the performance of NFP 3D-NP GS-MG with a low potential of 1.682 V at 1000 mA/cm^2 holds significant relevance.

Conclusion

Harnessing strain engineering represents a formidable approach in tailoring catalyst reactivity. In our pursuit of enhancing catalytic performance, we introduced a groundbreaking gradient structure design within MGs. This innovative approach capitalizes on strain engineering to achieve remarkable improvements in catalytic activity. The advantages inherent in the gradient structure design are manifold: firstly, it enables the generation of exceedingly large surface strains; secondly, the structural stability of strain distribution is significantly enhanced; thirdly, facile attainment of higher specific surface areas is facilitated through dealloying processes.

In a compelling demonstration of our concept, we showcased the deployment of NFP 3D-NP GS-MG electrodes in an integrated water-splitting cell. Astonishingly, these electrodes achieved water-splitting current densities of 10 mA/cm^2 and 1000 mA/cm^2 with impressively low voltage requirements of only 1.378 V and 1.682 V, respectively. This achievement marks a watershed moment in electrocatalysis, achieving the breakthrough among the performance of water splitting in alkaline media to date. Our groundbreaking work not only represents a paradigm shift in MG catalytic material fabrication but also heralds a new era of ultrahigh efficiency and stability in energy conversion applications. By leveraging the gradient structure design strategy, we pave the way for the widespread adoption of MGs as catalytic materials, promising a future characterized by unparalleled performance and durability.

Experimental section

Synthesis of MG wires (GS-MGs)

The precursor alloys ($Ni_{40}Fe_{40}P_{20}$, $Fe_{39}Ni_{39}B_{10.07}Si_{2.75}Nb_{2.3}P_{6.88}$, $Ni_{77}P_{23}$, $Co_{63}Fe_4Si_{5.6}B_{22.4}Nb_5$ and $Pd_{40}Ni_{10}Cu_{30}P_{20}$) were melted in a vacuum arc furnace and then cast into a bar with diameter of 5 mm by the copper-mold suction method in the high purity argon atmosphere. The alloy bars were subsequently cut into 5–7 mm in length by an electric discharge machine. After the sandpapers were used to remove the oxide layer from the surface. The precursor alloy ingots were first melted with a glass tube (made in high-borate borosilicate glass, the bottom of glass tube was designed as a pointed nose shape for convenient traction) into the molten pool by the inductors in the vacuum chamber (the inductors are made of single-turn Cu coil and the ultra-high frequency heating source of 400 kHz). The melting point of the alloy is within the supercooled liquid region of the glass tube, so the molten alloy causes the significant softening of the tube. Under a traction force, the melting alloy along the viscous glass tube is drawn to form the continuous amorphous microwires by the cooling device and then is wound by a roller for commercial application. The speed of the traction is about 35–75 m min^{-1} with the diameter of $\sim$ 35 μm.

Synthesis of NFP MG

The NFP MG ribbons with the same chemical composition were prepared by melt-spinning method using a Cu wheel (the revolving speed of 50 m s^{-1}) in an argon atmosphere.

Synthesis of 3D-NP GS-MG

First, NFP GS-MG wires were etched into an acid solution (1 M H_2SO_4) and test the LSV curve with three-electrode system. Then, find the corrosion potential according to the curve. The voltage and dealloying time were set according to the method of potentiostat. Finally, the 3D-NP GS-MGs were taken out, washed with ethanol with ultrasonic cleaner, and dried for later use.

Preparation of TEM samples

A protective layer of Pt was firstly deposited on the surface of the wire. Then, a U-shaped groove plate was dug along the Pt protective layer with the thickness of about 1 μm. The one end of thick plate was fixed by manipulator with Pt, and the other end of the original sample was cut by focused ion beam (FIB, FEI LD Helios G5 UX) with the length of 6 μm. After cutting, the sample was transferred to a copper wire and then gradually thinned by FIB. During this process, the FIB current is continuously reduced as the thickness of the thin region decreases, until the thickness of the thin region meets the TEM test requirements (50 $\sim$ 70 nm).

Structural characterizations

XRD (BRUKER-D8-ADVANCE with a Cu-K_α radiation source and a wavelength λ = 1.5418 Å, Germany) was utilized to determine the amorphous structures of the microwires. The sample morphology was investigated with a SEM (IT500). TEM observations were performed in a FEI Tecnai G2 F30 S-Twin TEM operated at 300 kV, with the element distribution of the wires was conducted by EDS. The thermal analysis was conducted using a DSC (TA Q800) with a heating rate of 5 K min^{-1}. XPS (Thermo Fisher ESCALAB XI+) analysis was performed with a Phoibos150 MCD-9 probe spectrometer with a monochromatic Al (300 W) K_α X-ray line source directed 35° with respect to the sample surface.

Nano-indentation tests

The nano-indentation tests were conducted using the Bruker/TI980 system, which integrates a high-resolution optical microscope and an in-situ scanning probe microscopy. The sample stage has a lateral movement range of 250 mm × 150 mm. Prior to testing, samples were vertically embedded in epoxy resin and subjected to a curing process. The specimens were then polished to a high finish to prepare them for nanoindentation. During the testing procedure, precise positioning was achieved through the combined use of the high-resolution optical microscopy and the in-situ scanning probe microscopy. An array-based indentation

mode was employed, ensuring accurate test initiation at the sample edges and maintaining consistent spacing between indentations across the sample.

Electrochemical measurements

After the detailed characterization, both OER and HER were conducted in an alkaline solution (1 M KOH) to test the catalytic performance. The electrochemical measurements were conducted by a standard three-electrode cell with the connection of an electrochemical workstation. As-synthesized NFP 3D-NP GS-MG electrode was employed as the working electrode. A commercial electrode (Pt for HER, RuO_2 for OER) was applied as the counter electrode. Hg/HgO electrode was utilized as the reference electrode. The potentials were converted to RHE by the equation, $E_{RHE} = E_{Hg/HgO} + 0.059\ pH + 0.098$ V-iR. For OER, high purity oxygen was bubbled through the electrolyte to saturate it and to ensure the O_2/H_2O equilibrium at 1.23 V vs RHE during the measurement. For HER, high purity nitrogen was bubbled through the electrolyte to remove the oxygen dissolved in solution 30 min prior to the measurements, as well as during the measurements. Cyclic Voltammetry (CV) measurements at a scan rate of 100 mV s^{-1} were performed for 20 cycles prior to conducting Linear Sweep Voltammetry (LSV) at a scan rate of 5 mV s^{-1} for characterizing the OER and HER electro-catalytic activity of each sample. The Electrochemical Impedance Spectroscopy (EIS) was measured at the open circuit potentials of each sample from 100 kHz to 0.01 Hz with an AC voltage amplitude of 5.0 mV. The CV was recorded in a narrow non-Faradaic potential window at different scan rates (20, 40, 60, 80, and 100 mV s^{-1}) to obtain electrical double layer capacitance (C_{dl}) and to estimate electrochemically active surface areas (ECSAs). The stability test was carried out by chronoamperometry to record the current density versus time curve at a fixed potential for 100 h.

DFT calculations

DFT calculations were performed by using the Vienna ab initio Simulation Package (VASP) [54–56]. The exchange and correlation energy were described by using the generalized general gradient approximation with the Perdew–Burke–Ernzerhof formalism (GGA-PBE) [57]. The electron-nuclei interaction was described by the Projector-Augmented Wave (PAW) pseudopotential [54]. The energy cutoff for the plane-wave basis was set to 400 eV. The convergence criteria in our DFT calculation were 1×10^{-5} eV and 0.05 eV $Å^{-1}$ for electronic and ionic optimization. The Gamma-only sampling of the electronic Brillouin zone for adsorbate geometry relaxation and $2 \times 2 \times 2$ k-point mesh for accurate electronic structure calculations.

The monolithic MG slab models were built by using Ab initio molecular dynamics (AIMD) simulations. To obtain an amorphous surface configuration, the NFP ($Ni_{40}Fe_{40}P_{20}$) glass-forming sample containing 100 atoms was melt via AIMD simulation with 6 ps time length (3 fs time step) with Nosé-Hoover thermostat at 2000 K to remove the internal stress [58]. We randomly take the MG model from AIMD trajectory for every 300 fs to obtain the amorphous MG. The vacuum layer is set to 20 Å in the z direction to minimize possible interactions between the replicated cells. The sampling of adsorption site also follows the composition of MG with the preference of 40 %, 40 % and 20 % on Ni, Fe and P.

Oxygen evolution reaction (OER)

The OER is assumed to involve four elementary reaction steps:

$$* + H_2O \leftrightarrow *OH + H^+ + e^- \quad \text{(S1)}$$

$$*OH \leftrightarrow *O + H^+ + e^- \quad \text{(S2)}$$

$$*O + H_2O \leftrightarrow *OOH + H^+ + e^- \quad \text{(S3)}$$

$$*OOH \leftrightarrow * + O_2 + H^+ + e^- \quad \text{(S4)}$$

where * represents the catalytic active sites. OH*, O* and OOH* represent the oxygen intermediates. The free energy of proton-electron pair was set as the chemical potential of $1/2H_2$ [59]. Since the energy of O_2 cannot be accurately calculated using DFT, we make the following approximation:

$$G_{O_2} = \left(2G_{O_2} - 2G_{H_2} - 4.92\text{eV}\right) \quad \text{(S5)}$$

The standard free energy change of each elementary step can be obtained by:

$$\Delta G_1 = \left(2G_{*OH} + 1/2G_{H_2}\right) - \left(G_* + G_{H_2O}\right) \quad \text{(S6)}$$

$$\Delta G_2 = \left(2G_{*O} + 1/2G_{H_2}\right) - G_{OH} \quad \text{(S7)}$$

$$\Delta G_3 = \left(G_{*OOH} + 1/2G_{H_2}\right) - \left(G_{*O} + G_{H_2O}\right) \quad \text{(S8)}$$

$$\Delta G_4 = \left(G_* + 1/2G_{H_2} + G_{O_2}\right) - G_{*OOH} \quad \text{(S9)}$$

In addition, we also performed thermodynamic corrections on the adsorption state free energy:

$$G = E + E_{ZPE} - T \cdot S \quad \text{(S10)}$$

where E is the corresponding electronic energy change calculated at DFT level, E_{ZPE} is the zero-point energy correction, S is the vibrational entropy.

The theoretical overpotential η can be calculated by:

$$\eta = \frac{\text{Max}[\Delta G_1, \Delta G_2, \Delta G_3, \Delta G_4]}{e}\text{-}1.23\text{V} \quad \text{(S11)}$$

where 1.23 V is the equilibrium potential of the reaction.

Hydrogen evolution reaction (HER)

The hydrogen adsorption energy (ΔG_H) is calculated by:

$$\Delta G_H = G_{*H} - \left(G_* + 1/2G_{H_2}\right) \quad \text{(S12)}$$

where G_{*H}, G_*, G_{*H2} are the total energies of the H atom adsorbed on the NFP surface, the individual NFP structure, and the gaseous H_2 molecule, respectively. G_{*H2} is calculated as −6.90 eV.

In an alkaline medium, the reaction formula for the HER is represented as:

$$\text{Volmer step: } H_2O + e^- \rightarrow *H + OH^- \quad \text{(S13)}$$

$$\text{Heyrovsky step: } H_2O + e^- + H* \rightarrow H_2 + OH^- \quad \text{(S14)}$$

Author contributions

C.Q. P., and T. F. conceived the idea and supervised all the aspects of the research. T. F., S.Q. C., H. H., B.A. S., and C. Z.

supportedtheprojectasanexpert.C.Q.P.,J.Y.X.,Y.Y.Q.,and G.N.Y.fabricatedthesamplesandcarriedoutthemeasurements. C.Q.P.,M.Y.Y.,Y.Y.Q.,G.N.Y.,performedthematerialschar-acterizations.M.Y.Y.,C.Z.,S.D.F.,andY.X.C.performedthe DFTcalculations.C.Q.P.,J.Y.X.,E.J.K.,D.W.,X.K.M.,G.N. Y.,S.L.,andG.W.evaluatedthedataandinterpretedtheresults. C.Q.P.,T.F.,C.Z.,andS.Q.C.wrotethepaper,andallauthors discussedtheresultsandworkedonthepaper.

CRediT authorship contribution statement

Chaoqun Pei: Writing – review & editing, Writing – original draft, Methodology, Formal analysis, Data curation, Conceptual-ization. **Shuangqin Chen:** Writing – review & editing, Formal analysis, Data curation. **Jiuyuan Xie:** Methodology, Formal analysis. **Shidong Feng:** Writing – review & editing, Methodol-ogy. **Mingyuan Yu:** Methodology. **Cheng Zhan:** Writing – review & editing, Methodology. **Yuyang Qian:** Methodology. **Guannan Yang:** Writing – review & editing, Methodology. **Yuxuan Chen:** Methodology. **Si Lan:** Writing – review & editing. **Erjun Kan:** Writing – review & editing, Methodology, Conceptualization. **Di Wang:** Writing – review & editing, Methodology. **Xiaoke Mu:** Writing – review & editing, Methodology. **Horst Hahn:** Writing – review & editing. **Baoan Sun:** Writing – review & editing, Writing – original draft, Methodology, Conceptualization. **Gerhard Wilde:** Writing – review & editing. **Tao Feng:** Writing – review & edit-ing, Writing – original draft, Data curation, Conceptualization.

Data availability

Data will be made available on request.

Declaration of competing interest

Theauthorsdeclarethattheyhavenoknowncompeting financialinterestsorpersonalrelationshipsthatcouldhave appearedtoinfluencetheworkreportedinthispaper.

Acknowledgements

ThisworkwassupportedbytheNationalNaturalScience FoundationofChina(Nos.52192602,62488201, 52101195,12261160364,52222104,51571119),theNational KeyR&DProgramofChina(No.2021YFB3802800, 2018YFA0703603),theGuangdongBasicandAppliedBasic ResearchFoundation(2023A1515110145),theChinaPostdoc-toralScienceFoundation(2024M762276),theFundamental ResearchFundsfortheCentralUniversities(Nos. 30919011404,30920021156,30919011107),theNaturalScience FoundationofJiangsuProvince(GrantNo.BK20230098, BK20200019),theStrategicPriorityResearchProgramofChinese AcademyofSciences(GrantNo.XDB30000000),andtheFund-ingofNJUST(No.TSXK2022D002).T.F.acknowledgesthesup-portfromQingLanprojectandthedistinguishedprofessor project of Jiangsu province.

References

[1] M.S. Dresselhaus, I. Thomas, Nature 414 (2001) 332 337. https://doi.org/10.1038/35104599.
[2] W.J. Jiang et al., Acc. Chem. Res. 53 (2020) 1111 1123. https://doi.org/10.1021/acs.accounts.0c00127.
[3] Z.W. Seh et al., Science 355 (2017) eaad4998. https://doi.org/10.1126/science.aad4998.
[4] M. Schalenbach et al., Int. J. Electrochem. Sci. 13 (2018) 1173 1226. https://doi.org/10.20964/2018.02.26.
[5] S. Lan et al., Nat. Mater. 20 (2021) 1347 1352. https://doi.org/10.1038/s41563-021-01152-7.
[6] J. Wang et al., Nat. Commun. 10 (2019) 1 11. https://doi.org/10.1038/s41467-019-13519-1.
[7] X. Zhang et al., Nat. Catal. 1 (2018) 460 468. https://doi.org/10.1038/s41929-018-0072-y.
[8] G. Chen et al., Adv. Mater. 31 (2019) 1900883. https://doi.org/10.1002/adma.201900883.
[9] Z.J. Wang et al., Adv. Mater. 32 (2020) 1906384. https://doi.org/10.1002/adma.201906384.
[10] F.Y. Gao et al., Nat. Catal. (2022) 1 13. https://doi.org/10.1038/s41929-022-00862-8.
[11] S. Anantharaj et al., Small 16 (2020) 1905779. https://doi.org/10.1002/smll.201905779.
[12] H. Xu et al., Coor. Chem. Rev. 418 (2020) 213374. https://doi.org/10.1016/j.ccr.2020.213374.
[13] C. Chen et al., Science 343 (2014) 1339 1343. https://doi.org/10.1126/science.1249061.
[14] L. Zhang et al., Science 349 (2015) 412 416. https://doi.org/10.1126/science.aab0801.
[15] L. Bu et al., Science 354 (2016) 1410 1414. https://doi.org/10.1126/science.aah6133.
[16] M. Luo et al., Nat. Rev. Mater. 2 (2017) 1 13. https://doi.org/10.1038/natrevmats.2017.59.
[17] M. Zhang et al., Energy Mater. 4 (2024) 400028. https://doi.org/10.20517/energymater.2023.101.
[18] P. Strasser et al., Nat. Chem. 2 (2010) 454 460. https://doi.org/10.1038/nchem.623.
[19] Y. Yan et al., J. Am. Chem. Soc. 145 (2023) 24218 24229. https://doi.org/10.1021/jacs.3c08598.
[20] H. Chiriac et al., Prog. Mater Sci. 40 (1996) 333 407. https://doi.org/10.1016/S0079-6425(97)00001-7.
[21] F. Zhu et al., Phys. Rev. Lett. 119 (2017) 215501. https://doi.org/10.1103/PhysRevLett.119.215501.
[22] F. Zhu et al., Nat. Commun. 9 (2018) 3965. https://doi.org/10.1038/s41467-018-06476-8.
[23] D. Ma et al., Nat. Mater. 8 (2009) 30 34. https://doi.org/10.1038/nmat2340.
[24] W.H. Wang, Prog. Mater Sci. 57 (2012) 487 656. https://doi.org/10.1016/j.pmatsci.2011.07.001.
[25] Y.H. Sun et al., Nat. Rev. Mater. 1 (2016) 1 14. https://doi.org/10.1038/natrevmats.2016.39.
[26] L. Berthier et al., Phys. Today 69 (2016) 40 46. https://doi.org/10.1063/PT.3.3052.
[27] S.F. Swallen et al., Science 315 (2007) 353 356. https://doi.org/10.1126/science.1135795.
[28] J. Pan et al., Nat. Commun. 9 (2018) 1 9. https://doi.org/10.1038/s41467-018-02943-4.
[29] Q. Xiao et al., J. Appl. Phys. 113 (2013) 083514. https://doi.org/10.1063/1.4793562.
[30] H. Chiriac et al., Phys. Rev. B 52 (1995) 10104. https://doi.org/10.1103/PhysRevB.52.10104.
[31] Y. Tang et al., Nat. Commun. 13 (2022) 1 11. https://doi.org/10.1038/s41467-022-29821-4.
[32] J. Wang et al., Sci. Adv. 8 (2022) eabl9271. https://doi.org/10.1126/sciadv.abl92.
[33] K. Zhang et al., Sci. China Chem. 62 (2019) 417 429. https://doi.org/10.1007/s11426-018-9441-4.
[34] F. Song et al., ACS Cent. Sci. 5 (2019) 558 568. https://doi.org/10.1021/acscentsci.9b00053.
[35] Q. Yao et al., Angew. Chem. 131 (2019) 14121 14126. https://doi.org/10.1002/ange.201908092.
[36] Y.Q. Wu et al., Adv. Mater. 31 (2019) 1900178. https://doi.org/10.1002/adma.201900178.

[37] P. Zhai et al., Nat. Commun. 12 (2021) 4587. https://doi.org/10.1038/s41467-021-24828-9.
[38] L. Yu et al., Nano Energy 41 (2017) 327 336. https://doi.org/10.1016/j.nanoen.2017.09.045.
[39] Z. Chen et al., Adv. Energy Mater. 9 (2019) 1803918. https://doi.org/10.1002/aenm.201803918.
[40] H. Zhang et al., Adv. Funct. Mater. 28 (2018) 1706847. https://doi.org/10.1002/adfm.201706847.
[41] H. Xu et al., Adv. Energy Mater. 10 (2020) 1902714. https://doi.org/10.1002/aenm.201902714.
[42] L. Yu et al., Energ. Environ. Sci. 10 (2017) 1820 1827. https://doi.org/10.1039/C7EE01571B.
[43] W. Zhang et al., Int. J. Hydrogen Energy 47 (2022) 1633 1643. https://doi.org/10.1016/j.ijhydene.2021.10.223.
[44] Y. Wang et al., Angew. Chem. 134 (2022) e202116233. https://doi.org/10.1002/ange.202116233.
[45] L. Qi et al., Adv. Funct. Mater. 32 (2022) 2107179. https://doi.org/10.1002/adfm.202107179.
[46] J. Jayabharathi et al., Phys. Chem. Chem. Phys. 25 (2023) 8992 9019. https://doi.org/10.1039/D2CP05522H.
[47] A. Saad et al., Small 18 (2022) 2104303. https://doi.org/10.1002/smll.202104303.
[48] G. Zhou et al., Adv. Funct. Mater. 32 (2022) 2107608. https://doi.org/10.1002/adfm.202107608.
[49] H. Ashassi-Sorkhabi et al., Corros. Sci. 77 (2013) 185 193. https://doi.org/10.1016/j.corsci.2013.07.046.
[50] F. Zhao et al., J. Mater. Chem. A 11 (2023) 276 286. https://doi.org/10.1039/d2ta06514b.
[51] C. Hu et al., Angew. Chem. Int. Ed. 60 (2021) 19774 19778. https://doi.org/10.1002/anie.202103888.
[52] Y. Tan et al., Adv. Mater. Interfaces 4 (2017) 1601086. https://doi.org/10.1002/admi.201601086.
[53] Z. Zhuang et al., Nat. Commun. 10 (2019) 1 10. https://doi.org/10.1038/s41467-019-12885-0.
[54] P.E. Blöchl, Phys. Rev. B 50 (1994) 17953. https://doi.org/10.1103/PhysRevB.50.17953.
[55] G. Kresse et al., Comput. Mater. Sci 6 (1996) 15 50. https://doi.org/10.1016/0927-0256(96)00008-0.
[56] G. Kresse et al., Phys. Rev. B 59 (1999) 1758. https://doi.org/10.1103/PhysRevB.59.1758.
[57] J.P. Perdew et al., Phys. Rev. Lett 77 (1996) 3865. https://doi.org/10.1103/PhysRevLett.77.3865.
[58] S. Nosé, J. Chem. Phys. 81 (1984) 511 519. https://doi.org/10.1063/1.447334.
[59] J.K. Nørskov et al., J. Phys. Chem. B 108 (2004) 17886 17892. https://doi.org/10.1021/jp047349j.